

Computational Magnetohydrodynamics

Manlin Chawla

Cavendish Laboratory, Department of Physics, J J Thomson Avenue, Cambridge. CB3 0HE

1. Introduction

When a gas is heated to a high temperature of approximately 10,000K [1], electrons can be stripped away from the atoms they are attached to forming an ionized gas which we call plasma. Plasma is made up of positively charged ions and negatively charged electrons. Plasma is often referred to as the 'fourth state of matter' and comprises over 99% of visible matter in the universe [1]. As a result, the behaviour and properties of plasma are of interest to scientists across multiple disciplines and plasma physics is an exciting and growing area of active research. From a scientific point of view studying plasma can help us understand various astro and geophysical phenomena's such as stellar evolution, cosmic jets and lightning. From a technological point of view, it can help us develop new technologies with far-reaching applications such as Tokamaks which can make nuclear fusion a feasible source of energy, which is the aim of research projects such as ITER [2].

Due to the vast development in computing resources and often the high temperatures and short lifetimes of plasma states, numerical simulations are increasingly being used as a powerful alternative to experimental plasma research [3]. A whole hierarchy of mathematical models describing plasma exists, covering both the atomistic and continuum length scales. The motion of plasma is dominated by electric and magnetic fields and not just pressure changes [4], therefore each model describing plasma is built from coupling equations of gas dynamics with Maxwell's equations.

At the microscopic level, an N -body model can be used to model N plasma particles with Newton's equations of motion. In reality, N can be very large, simulating the interactions between each particle through direct calculation quickly becomes expensive. On the mesoscopic scale, kinetic models such as the Vlasov-Maxwell equations are used to model plasma. In a kinetic model each particle species s is described by a function $f(\mathbf{x}, \mathbf{v}, t)$ which describes the probability of a particle being at the point (\mathbf{x}, \mathbf{v}) in 6 dimensional phase space [5].

In this study, we consider a fluid description of plasma. The magnetohydrodynamic (MHD) equations combine

the Euler and Maxwell equations, these are the basic equations used for studying the behaviour of electrically conducting fluids in the presence of magnetic fields. When viscous, resistive, thermal conductivity and relativistic effects are neglected ($v \ll c$) and plasma is assumed to be fully ionized, the reduced model is referred to as the compressible ideal MHD system. The objective of this paper is to numerically solve the compressible ideal MHD equations using a high-resolution method. Solutions are presented in both 1D and 2D and the effects of divergence cleaning have been investigated.

The structure of the rest of the paper is as follows. Section 2 provides an outline of the literature surrounding the field. Section 3 details the mathematical equations used to describe the physical problem and the numerical methods used to numerically solve them. In section 4 a series of test cases are presented to validate our implementation. Conclusions are provided in Section 5.

2. Literature Review

In this section, we review the work of researchers who have computationally solved the ideal MHD equations. This research area has a deep literature background so only a representative sample of works have been included.

The ideal MHD equations form a set of non-linear hyperbolic equations. Over the years many finite volume schemes have been developed to solve hyperbolic systems of conservation laws. Godunov's method and its higher-order extensions have remained a popular method for solving the Euler equations due to their robustness, shock-capturing properties and ability to achieve a high resolution at discontinuities [6]. Many researchers have worked on extending Godunov-type methods (which were originally developed for solving problems in shock hydrodynamics) to numerically solve the ideal MHD equations.

Brio and Wu [7] were amongst the first to apply a Godunov-type method to solve the MHD equations. They used Roe's approximate solver to numerically solve the ideal MHD equations for the special case

where the ratio of specific heats $\gamma = 2$. Other authors such as Balsara [8] and Cargo and Gallice [9] have constructed Roe-type schemes without any constraints on the value of γ . These papers demonstrate that Roe-type schemes have several advantages, for example, non-physical oscillatory behaviour is not generated in the solution and there is high resolution at discontinuities. However, this type of solver requires eigendecomposition which becomes complicated and time consuming for the MHD equations. Moreover, Einfeldt et al [10] proved that for certain Riemann problems Roe's scheme does not preserve positivity.

A positivity preserving numerical method for solving the MHD equations is highly desirable. This is motivated by the fact that for the MHD systems with plasma at low density, the internal energy often becomes less dominant than kinetic and in some cases, magnetic energy [11]. As a result, numerical simulations can start to produce solutions containing negative density and pressure. As soon as such values appear, the corresponding discrete problem becomes ill-posed and the system is no longer hyperbolic [12] and unphysical behaviour is generated in the solutions.

Several efforts have been made to design positivity preserving schemes for solving the ideal MHD equations. Janhunen [13] considered a modified MHD system that allows for magnetic monopoles. This is accounted for by including source terms in the induction equation. Through discretizing this modified system, Janhunen developed a 1D HLL type Riemann solver and demonstrates its positivity preserving properties through numerical experiments. Linde [14] developed a two-state HLL approximate Riemann solver which resolves discontinuities sharply using a geometric interpretation of the Rankine-Hugoniot conditions. Linde's solver is not tied to any specific set of governing equations but the paper demonstrates its use in solving 1D test problems in ideal MHD. Gurski [15] used the HLLC solver devised by Toro, Spruce and Speares [16] for the Euler equations to develop a 'smoothed MHD-HLLC' solver which is shown to be a variant of Linde's solver. The smoothed variant has an advantage over Linde's scheme in that it includes an algorithm for choosing wave speeds that ensures the positivity of the solutions.

Alternatively, Li [17] extended Toro, Spruce and Speares HLLC solver [16] to the MHD equations and provides expressions for the intermediate states (in multiple dimensions) which are consistent with the integral form of the conservation laws of magnetohydrodynam-

ics. Wesenberg [18] extended Einfeldt's HLLE scheme [10] by introducing anti-diffusion terms to all waves apart from the fast waves.

Brio and Wu [7] rigorously proved that the ideal MHD equations are non-convex. A consequence of this is that wave structures such as Alfvén waves, compound waves and rotational discontinuities (which do not exist in the Euler equations) can exist in MHD solutions [11]. Miyoshi and Kusano [11] present a HLLD Riemann solver consisting of 4 intermediate states all of which can be obtained analytically through considering the jump conditions. The paper demonstrates the schemes ability to exactly resolve isolated discontinuities and it is proven analytically that the scheme preserves the positivity of solutions provided that the maximum wave signals are properly satisfied.

The ideal MHD equations include a divergence-free constraint on the magnetic field. Mathematically, if the initial conditions satisfy the divergence constraint then so will the exact solutions for all future times. However, due to discretization errors, most multi-dimensional MHD simulations have a non-zero divergence of the magnetic field which leads to numerical instabilities and non-physical features in the solutions [19] even if the condition is satisfied at $t = 0$. Many numerical techniques have been proposed to enforce the divergence-free conditions in numerical simulations. Dedner et al [20] derived a divergence cleaning method which couples the divergence constraint with the evolution equations by introducing a generalized lagrangian multiplier. In their paper, they present a mixed hyperbolic/parabolic correction and show that it will evolve away divergence errors with the maximum admissible wave speed of the system. Evans and Hawley [21] presented the constrained transport approach where the divergence-free condition is inherent within the method itself. This technique requires a staggered grid approach where some magnetic field components are stored at cell centres and others at cell corners. Powell [22] introduced an 8-wave method, this involves modifying the MHD equations to include source terms that are proportional to $\nabla \cdot B$. These source terms are evaluated at every time step and any local divergence errors created are convected away.

3. Mathematical and Numerical Formulation

A. Ideal MHD Equations

The compressible ideal magnetohydrodynamic equations describe the motion of flow of electrically conducting fluids such as plasma under the presence of a

magnetic field when the effects of electrical resistivity ($\eta = 0$), viscosity, thermal conductivity and relativistic effects ($v \ll c$) are neglected. The ideal MHD equations in conservation law form are given by [4]:

$$\frac{\partial \rho}{\partial t} + \nabla \cdot (\rho \mathbf{v}) = 0 \quad (1)$$

$$\frac{\partial \rho \mathbf{v}}{\partial t} + \nabla \cdot \left[\rho \mathbf{v} \otimes \mathbf{v} + \left(p + \frac{1}{2} B^2 \right) \mathbf{I} - \mathbf{B} \otimes \mathbf{B} \right] = 0 \quad (2)$$

$$\frac{\partial U}{\partial t} + \nabla \cdot \left[\left(U + p + \frac{1}{2} B^2 \right) \mathbf{v} - (\mathbf{v} \cdot \mathbf{B}) \mathbf{B} \right] = 0 \quad (3)$$

$$\frac{\partial \mathbf{B}}{\partial t} + \nabla \cdot (\mathbf{B} \otimes \mathbf{v} - \mathbf{v} \otimes \mathbf{B}) = 0 \quad (4)$$

with

$$\nabla \cdot \mathbf{B} = 0$$

where ρ is density, \mathbf{v} is the velocity vector, p is the pressure, $\mathbf{B} = (B_x, B_y, B_z)$ is the magnetic field vector and U is the total energy of the system given by

$$U = \rho \epsilon + \frac{1}{2} \rho v^2 + \frac{1}{2} B^2$$

where ϵ is the specific internal energy. In ideal MHD we are considering completely ionised plasma, hence we can use the ideal gas equation of state

$$p = (\gamma - 1) \rho \epsilon$$

to close this system of equations, where γ is the ratio of specific heats. For this system of equations, the conservative variables \mathbf{U} and the primitive variables \mathbf{W} are defined as

$$\mathbf{U} = \begin{bmatrix} \rho \\ \rho \mathbf{v} \\ U \\ \mathbf{B} \end{bmatrix}, \quad \mathbf{W} = \begin{bmatrix} \rho \\ \mathbf{v} \\ p \\ \mathbf{B} \end{bmatrix}$$

B. 1D Considerations

We first consider how to treat this system of equations in 1D. Expanding out the derivatives and writing the equations in vector form we have:

$$\frac{\partial \mathbf{U}}{\partial t} + \frac{\partial \mathbf{f}(\mathbf{U})}{\partial x} + \frac{\partial \mathbf{g}(\mathbf{U})}{\partial y} + \frac{\partial \mathbf{h}(\mathbf{U})}{\partial z} = 0 \quad (5)$$

where $\mathbf{f}(\mathbf{U})$, $\mathbf{g}(\mathbf{U})$, $\mathbf{h}(\mathbf{U})$ are the flux vectors in the spatial direction of the corresponding derivatives. The 1D equations must satisfy [4]

$$\frac{\partial \mathbf{g}(\mathbf{U})}{\partial y} = \frac{\partial \mathbf{h}(\mathbf{U})}{\partial z} = 0 \quad (6)$$

This does not allow us to assume $B_y = B_z = 0$ and $v_y = v_z = 0$. This is due to the magnetic field evolution equation (4). Examining this component-wise we see that B_y, B_z, v_y, v_z are allowed to evolve but must satisfy the condition given in (6). Furthermore it is important to note that for the x -derivative we have

$$\begin{aligned} \frac{\partial B_x}{\partial t} + \frac{\partial}{\partial x} (B_x v_x - v_x B_x) &= \frac{\partial B_x}{\partial t} = 0 \\ \implies B_x &= \text{constant} \end{aligned}$$

and does not evolve. This allows us to write the 1D system as follows:

$$\frac{\partial \mathbf{U}}{\partial t} + \frac{\partial \mathbf{f}(\mathbf{U})}{\partial x} = 0 \quad (7)$$

with

$$\mathbf{f}(\mathbf{U}) = \begin{bmatrix} \rho v_x^2 + p + \frac{1}{2} B^2 - B_x B_x \\ \rho v_x v_y - B_x B_y \\ \rho v_x v_z - B_x B_z \\ (U + p + \frac{1}{2} B^2) v_x - (\mathbf{v} \cdot \mathbf{B}) B_x \\ 0 \\ B_y v_x - B_x v_y \\ B_z v_x - B_x v_z \end{bmatrix} \quad (8)$$

Before proceeding, we consider the eigenstructure of the ideal MHD equations, firstly to confirm the system is hyperbolic, secondly to gain an insight into the wave structures in the solution and thirdly to compute the associated wave speeds. Writing the equations in primitive form we have [4]

$$\frac{\partial \mathbf{W}}{\partial t} + A(\mathbf{W}) \frac{\partial \mathbf{W}}{\partial x} = 0$$

where $A(\mathbf{W})$ is the matrix

$$\begin{bmatrix} v_x & \rho & 0 & 0 & 0 & 0 & 0 \\ 0 & v_x & 0 & 0 & 1/\rho & B_y/\rho & B_z/\rho \\ 0 & 0 & v_x & 0 & 0 & -B_x/\rho & 0 \\ 0 & 0 & 0 & v_x & 0 & 0 & -B_x/\rho \\ 0 & \rho c_s^2 & 0 & 0 & v_x & 0 & 0 \\ 0 & B_y & -B_x & 0 & 0 & v_x & 0 \\ 0 & B_z & 0 & -B_x & 0 & 0 & v_x \end{bmatrix}$$

Computing the eigenvalues, we have

$$\begin{aligned} \lambda_{1,7} &= v_x \pm c_f \\ \lambda_{2,6} &= v_x \pm c_a \\ \lambda_{3,5} &= v_x \pm c_{sl} \\ \lambda_4 &= v_x \end{aligned}$$

where the Alfvén speed c_a and the slow and fast magneto-acoustic speeds c_{sl} and c_f are given by

$$c_a = \frac{B}{\sqrt{\rho}}$$

$$c_{f,sl}^x = \sqrt{\frac{1}{2} \left[c_s^2 + c_a^2 \pm \sqrt{(c_s^2 + c_a^2)^2 - 4 \frac{c_s^2 B_x^2}{\rho}} \right]} \quad (9)$$

The sound speed c_s is given by

$$c_s = \sqrt{\frac{\gamma p}{\rho}}$$

The quantities λ_1 - λ_7 are all real so the ideal MHD is a hyperbolic system. These correspond to an entropy wave travelling with speed λ_1 , two Alfvén waves travelling with speed $\lambda_{2,6}$ and four magneto-acoustic waves, two "fast" and two "slow" waves travelling with speeds $\lambda_{1,7}$ and $\lambda_{3,5}$ respectively [22]. Note, that as degenerate wave cases exist, the ideal MHD system is non-strictly hyperbolic.

C. Hyperbolic Solver

The discretized form of (7) in a finite volume framework is given by

$$\mathbf{U}_i^{n+1} = \mathbf{U}_i^n - \frac{\Delta t}{\Delta x} (\mathbf{F}_{i+\frac{1}{2}}^n(\mathbf{U}) - \mathbf{F}_{i-\frac{1}{2}}^n(\mathbf{U})) \quad (10)$$

For the 1D system, we can compute the time step as

$$\Delta t = \frac{C \Delta x}{a_{max}}$$

where a_{max} is the maximal wave speed given by

$$a_{max} = \max_i (|\mathbf{v}_i| + c_f)$$

To compute the intercell flux, we used the HLLC method proposed by Li [17]. This method consists of two intermediate states separated by a contact discontinuity and three waves splitting the $x - t$ plane into four constant states. The advantage of this approximate Riemann solver is that it is consistent with the underlying ideal MHD conservation laws and it can achieve a high resolution when resolving contact discontinuities. The wave speed estimates are taken to be

$$S_L = \min(v_{x,L}, v_{x,L}) - \max(c_{f,L}, c_{f,R})$$

$$S_R = \max(v_{x,L}, v_{x,L}) + \max(c_{f,L}, c_{f,R})$$

Following the notation used in the original reference, we consider a total pressure

$$p_T = p + \frac{1}{2} B^2$$

and consider the jump conditions across each wave to obtain the following expressions (11 - 17) for the intermediate states $K \in [L, R]$

$$S^* = v_x^* = \frac{\rho_R v_{x,R} (S_R - v_{x,R}) - \rho_L v_{x,L} (S_L - v_{x,L}) + p_{T,L} - p_{T,R} - B_{x,L}^2 + B_{x,R}^2}{\rho_R (S_R - v_{x,R}) - \rho_L (S_L - v_{x,L})} \quad (11)$$

$$p_T^* = \rho (S_K - v_{x,K}) (v_x^* - v_{x,K}) + p_T - B_{x,K}^2 + (B_{x,K}^*)^2 \quad (12)$$

$$\rho_K^* = \rho_K \frac{S_K - v_{x,K}}{S_K - S^*} \quad (13)$$

$$(\rho v_x)_K^* = \rho_K^* S^* \quad (14)$$

$$(\rho v_y)_K^* = \rho_K v_{y,K} \frac{S_K - v_{x,K}}{S_K - S^*} - \frac{B_{x,K}^* B_{y,K}^* - B_{x,K} B_{y,K}}{S_K - S^*} \quad (15)$$

$$(\rho v_z)_K^* = \rho_K v_{z,K} \frac{S_K - v_{x,K}}{S_K - S^*} - \frac{B_{x,K}^* B_{z,K}^* - B_{x,K} B_{z,K}}{S_K - S^*} \quad (16)$$

$$U_K^* = U_K \frac{S_K - v_{x,K}}{S_K - S^*} + \frac{p_T^* S^* - p_{T,K} v_{x,K} - [B_x^* (\mathbf{B} \cdot \mathbf{v})^* - B_{x,K} (\mathbf{B} \cdot \mathbf{v})]}{S_L - S^*} \quad (17)$$

To abide with the consistency with the underlying equations we define the rest of the intermediate quantities as

$$B_y^* = B_y^{\text{HLL}}$$

$$B_z^* = B_z^{\text{HLL}}$$

$$(\mathbf{B} \cdot \mathbf{v})^* = \mathbf{B}^{\text{HLL}} \cdot \mathbf{v}^{\text{HLL}}$$

The HLL quantities can be computed through

$$\mathbf{U}^{\text{HLL}} = \frac{S_R \mathbf{U}_R - S_L \mathbf{U}_L - (\mathbf{f}_R - \mathbf{f}_L)}{S_R - S_L}$$

Note that in 1D $B_x^* = B_{x,L}^* = B_{x,R}^* = B_{x,L} = B_{x,R} = B_x$ which is constant. When extending this scheme to multiple dimensions, we set

$$B_x^* = B_x^{\text{HLL}}$$

The inter-cell flux is computed using:

$$\mathbf{F}^{\text{HLLC}} = \begin{cases} \mathbf{f}_L & 0 \leq S_L \\ \mathbf{f}_L + S_L (\mathbf{U}_L^* - \mathbf{U}_L) & S_L \leq 0 \leq S^* \\ \mathbf{f}_R + S_R (\mathbf{U}_R^* - \mathbf{U}_R) & S^* \leq 0 \leq S_R \\ \mathbf{f}_R & S_R \leq 0 \end{cases} \quad (18)$$

The HLLC solver is first-order accurate, it can be combined with the MUSCL-Hancock approach to achieve second-order accuracy.

D. Second-Order Extension

The first step in the MUSCL-Hancock approach is data reconstruction. In this step, we consider piece-wise constant data in each cell and introduce slope reconstruction across the cell boundaries. Using first-order reconstruction, we replace the piece-wise constant data with a piece-wise linear function. The boundary extrapolated values are given by

$$\mathbf{U}_i^L = \mathbf{U}_i^n - \frac{1}{2}\Delta_i \quad \mathbf{U}_i^R = \mathbf{U}_i^n + \frac{1}{2}\Delta_i$$

The slope vector is defined as

$$\Delta_i = \frac{1}{2}(1 + \omega)\Delta_{i-\frac{1}{2}} + \frac{1}{2}(1 - \omega)\Delta_{i+\frac{1}{2}}$$

$$\Delta_{i-\frac{1}{2}} \equiv \mathbf{U}_i^n - \mathbf{U}_{i-1}^n; \quad \Delta_{i+\frac{1}{2}} \equiv \mathbf{U}_{i+1}^n - \mathbf{U}_i^n$$

$\omega \in [-1, 1]$ and is often taken to be 0. It is important to consider what happens at discontinuities, at these points the derivative does not exist and this can cause spurious oscillations in regions of steep gradients. In the TVD version of this scheme, slope limiting is used in the data reconstruction step. The slope vectors are replaced with limited slopes given by

$$\bar{\Delta}_i = \xi_i(r)\Delta_i \quad (19)$$

where r is defined as

$$r = \frac{u_i^n - u_{i-1}^n}{u_{i+1}^n - u_i^n} \quad (20)$$

and $\xi_i(r)$ is a slope limiter function. Some common slope limiters are [6]:

$$\xi_{\text{MINBEE}}(r) = \begin{cases} 0 & r \leq 0 \\ r & 0 \leq r \leq 1 \\ \min\{1, \xi_R(r)\} & r \geq 1 \end{cases}$$

$$\xi_{\text{VANALBADA}}(r) = \begin{cases} 0 & r \leq 0 \\ \min\left\{\frac{r(1+r)}{1+r^2}, \xi_R(r)\right\} & r \geq 0 \end{cases}$$

$$\xi_{\text{VANLEER}}(r) = \begin{cases} 0 & r \leq 0 \\ \min\left\{\frac{2r}{1+r}, \xi_R(r)\right\} & r \geq 0 \end{cases}$$

$$\xi_{\text{SUPERBEE}}(r) = \begin{cases} 0 & r \leq 0, \\ 2r & 0 \leq r \leq \frac{1}{2} \\ 1 & \frac{1}{2} \leq r \leq 1 \\ \min\{r, \xi_R(r), 2\} & r \geq 1 \end{cases}$$

where

$$\xi_R(r) = \frac{2}{1+r}$$

In the case of large changes, the slope limiter reverts to piece-wise constant data. Alternatively for smooth changes, the reconstructed data is used. In between these two extremes, a spectrum of limiting is used [4].

Next, the boundary extrapolated are evolved by $\frac{\Delta t}{2}$ as

$$\bar{\mathbf{U}}_i^L = \mathbf{U}_i^L - \frac{1}{2} \frac{\Delta t}{\Delta x} [\mathbf{F}(\mathbf{U}_i^R) - \mathbf{F}(\mathbf{U}_i^L)]$$

$$\bar{\mathbf{U}}_i^R = \mathbf{U}_i^R - \frac{1}{2} \frac{\Delta t}{\Delta x} [\mathbf{F}(\mathbf{U}_i^R) - \mathbf{F}(\mathbf{U}_i^L)]$$

Now we can use these values to compute the numerical intercell by solving a Riemann problem at the interface, using the HLLC flux

$$\mathbf{U}_L \equiv \bar{\mathbf{U}}_i^R \quad \mathbf{U}_R \equiv \bar{\mathbf{U}}_{i+1}^L$$

$$\mathbf{F}_{i+\frac{1}{2}} = \mathbf{F}_{i+\frac{1}{2}}^{\text{HLLC}}(\bar{\mathbf{U}}_i^R, \bar{\mathbf{U}}_{i+1}^L)$$

Finally, this numerical flux is used in the finite volume update formula.

$$\mathbf{U}_i^{n+1} = \mathbf{U}_i^n - \frac{\Delta t}{\Delta x} (\mathbf{F}_{i+\frac{1}{2}}^n(\mathbf{U}) - \mathbf{F}_{i-\frac{1}{2}}^n(\mathbf{U}))$$

E. 2D considerations

For the 2D MHD system we consider (5) and this time we impose that the 2D equations must satisfy

$$\frac{\mathbf{h}(\mathbf{U})}{\partial z} = 0$$

Repeating the same analysis and considering the magnetic field evolution equation component-wise we have

$$\frac{\partial B_i}{\partial t} + \frac{\partial}{\partial i}(B_i v_i - v_i B_i) = \frac{\partial B_i}{\partial t} = 0 \quad \text{for } i \in \{x, y\}$$

This allows us to write the flux vectors as

$$\mathbf{f}(\mathbf{U}) = \begin{bmatrix} \rho v_x^2 + p + \frac{1}{2}B^2 - B_x B_x \\ \rho v_x v_y - B_x B_y \\ \rho v_x v_z - B_x B_z \\ (U + p + \frac{1}{2}B^2) v_x - (\mathbf{v} \cdot \mathbf{B}) B_x \\ 0 \\ B_y v_x - B_x v_y \\ B_z v_x - B_x v_z \end{bmatrix}$$

$$\mathbf{g}(\mathbf{U}) = \begin{bmatrix} \rho v_y^2 + p + \frac{1}{2}B^2 - B_y B_y \\ \rho v_x v_y - B_x B_y \\ \rho v_y v_z - B_y B_z \\ (U + p + \frac{1}{2}B^2) v_y - (\mathbf{v} \cdot \mathbf{B}) B_y \\ 0 \\ B_x v_y - B_y v_x \\ B_z v_y - B_y v_z \end{bmatrix}$$

In our numerical methods, the following discretisation seems sensible for the finite volume method [4]

$$\mathbf{U}_{i,j}^{n+1} = \mathbf{U}_{i,j}^n - \frac{\Delta t}{\Delta x} (\mathbf{F}_{i+\frac{1}{2},j}^n(\mathbf{U}) - \mathbf{F}_{i-\frac{1}{2},j}^n(\mathbf{U})) - \frac{\Delta t}{\Delta y} (\mathbf{G}_{i,j+\frac{1}{2}}^n(\mathbf{U}) - \mathbf{G}_{i,j-\frac{1}{2}}^n(\mathbf{U}))$$

where we consider a computational grid with cells of size $\Delta x \times \Delta y$. However, this method can cause issues with stability and requires a CFL number

$$C = \frac{1}{2} C_{1D}$$

which is half of what is in 1D. As the timestep is proportional to the CFL number, this leads to a more computationally expensive integration scheme. Instead, we consider a dimensionally split approach where we update the x -direction first and then update the y -direction. This scheme is given by

$$\bar{\mathbf{U}}_{i,j} = \mathbf{U}_{i,j}^n - \frac{\Delta t}{\Delta x} (\mathbf{F}_{i+\frac{1}{2},j}^n(\mathbf{U}) - \mathbf{F}_{i-\frac{1}{2},j}^n(\mathbf{U}))$$

$$\mathbf{U}_{i,j}^n = \bar{\mathbf{U}}_{i,j} - \frac{\Delta t}{\Delta y} (\mathbf{G}_{i,j+\frac{1}{2}}^n(\bar{\mathbf{U}}) - \mathbf{G}_{i,j-\frac{1}{2}}^n(\bar{\mathbf{U}}))$$

This approach is consistent with the underlying PDE (in the limit $\Delta x \rightarrow 0$, $\Delta y \rightarrow 0$ and is useful as it allows for the diagonal propagation of information over a single time step. It should be noted that dimensional splitting is first-order accurate in time [4]. This approach allows us to consider a one-dimensional problem in the x and y directions. The new time step is now given by

$$\Delta t = \frac{C \min(\Delta x, \Delta y)}{a_{max}}$$

where the maximal wave speed in the system is given by

$$a_{max} = \max_{i,j} (|v_x| + c_f^x, |v_y| + c_f^y)$$

where c_f^x is given by (9) and

$$c_f^y = \sqrt{\frac{1}{2} \left[c_s^2 + c_a^2 + \sqrt{(c_s^2 + c_a^2)^2 - 4 \frac{c_s^2 B_y^2}{\rho}} \right]}$$

In the implementation, we include two ghost cells around the computational domain to enforce boundary conditions. The choice of the boundary conditions is problem dependant.

F. Divergence Cleaning Method

As discussed in section 2, numerical techniques which ensure divergence-free simulations are necessary for obtaining accurate results. One such method is the constrained transport method devised by Evans and Hawley [21]. This method involves using a staggered grid approach and storing some magnetic field components at cell centres and others at cell edges. In this study we consider the divergence cleaning approach devised by Dedner et Al [20] as it can be built directly upon any existing code. It requires one extra evolution equation and a few extra modifications. Although the constrained transport method is mathematically more accurate and does not depend on tunable parameters, the divergence cleaning approach is a lot simpler to implement.

In the divergence cleaning method, the divergence-free constraint is coupled to the evolution equation of the magnetic field by introducing a generalized Lagrangian multiplier ψ [20]

$$\frac{\partial \mathbf{B}}{\partial t} + \nabla \cdot (\mathbf{B} \otimes \mathbf{u} - \mathbf{u} \otimes \mathbf{B}) + \nabla \psi = 0$$

$$\mathcal{D}(\psi) + \nabla \cdot \mathbf{B} = 0$$

where $\mathcal{D}(\cdot)$ is a linear differential operator.

Dedner et Al [20] present various options for the choice of $\mathcal{D}(\psi)$, we use the mixed correction approach defined by

$$\mathcal{D}(\psi) = \frac{1}{c_h^2} \partial_t \psi + \frac{1}{c_p^2} \psi$$

The resulting system with the mixed correction becomes

$$\begin{aligned}\frac{\partial \rho}{\partial t} + \nabla \cdot (\rho \mathbf{v}) &= 0 \\ \frac{\partial \rho \mathbf{v}}{\partial t} + \nabla \cdot \left[\rho \mathbf{v} \otimes \mathbf{v} + \left(p + \frac{1}{2} B^2 \right) \mathbf{I} - \mathbf{B} \otimes \mathbf{B} \right] &= 0 \\ \frac{\partial U}{\partial t} + \nabla \cdot \left[\left(U + p + \frac{1}{2} B^2 \right) \mathbf{v} - (\mathbf{v} \cdot \mathbf{B}) \mathbf{B} \right] &= 0 \\ \frac{\partial \mathbf{B}}{\partial t} + \nabla \cdot (\mathbf{B} \otimes \mathbf{v} - \mathbf{v} \otimes \mathbf{B} + \psi \mathbf{I}) &= 0 \\ \frac{\partial \psi}{\partial t} + \nabla \cdot (c_h^2 \mathbf{B}) &= -\frac{c_h^2}{c_p^2} \psi\end{aligned}$$

Vides et Al [23] analyse the eigen-structure of this mixed GLM system and show that it has nine distinct real eigenvalues making the system hyperbolic. It can be shown that in this mixed GLM system the divergence errors are propagated away with a speed c_h and damped by the source term [23][20].

The speed c_h is the maximal admissible wave speed given by

$$c_h = \max_{i,j,k} (|v_x| + c_{f,x}, |v_y| + c_{f,y}, |v_z| + c_{f,z})$$

where $c_{f,x}$, $c_{f,y}$, $c_{f,z}$ are the fast magneto-acoustic speeds in the x, y, z respectively. The maximum timestep is given by

$$\Delta t = \frac{C \min(\Delta x, \Delta y, \Delta z)}{c_h}$$

where C is the CFL number such that $0 < C < 1$.

We now consider the modifications to the numerical method required in the x -direction. The changes to the y direction are analogous. In this new system, the variables B_x and ψ decouple from the rest of the system

$$\begin{aligned}\frac{\partial B_x}{\partial t} + \frac{\partial \psi}{\partial x} &= 0 \\ \frac{\partial \psi}{\partial t} + c_h^2 \frac{\partial B_x}{\partial x} &= -\frac{c_h^2}{c_p^2} \psi\end{aligned}$$

For our specific implementation used, these variables are not evolved in the MUSCL-Hancock Method. Instead the Godunov numerical flux for an arbitrary left and right states $(B_{x,L}, \psi_L)$ and $(B_{x,R}, \psi_R)$ can be computed exactly [23] and is given by $(\tilde{\psi}, c_h^2 \tilde{B}_x)$ where

$$\begin{aligned}\tilde{B}_x &= \frac{1}{2} (B_{x,L} + B_{x,R}) - \frac{1}{2c_h} (\psi_R - \psi_L) \\ \tilde{\psi} &= \frac{1}{2} (\psi_L + \psi_R) - \frac{c_h}{2} (B_{x,R} - B_{x,L})\end{aligned}$$

For the remaining system and 7 variables the MUSCL-Hancock HLLC solver is used but with the normal component of the magnetic field defined by \tilde{B}_x . The resulting numerical intercell flux for the full system with conserved variables $\mathbf{U} = (\rho, \rho \mathbf{v}, E, \mathbf{B}, \psi)^T$ is given by

$$\mathbf{F}_{i+\frac{1}{2},j} = \mathbf{F}_{i+\frac{1}{2},j}^{\text{HLLC}}(\mathcal{R}(\mathbf{U}_L, \mathbf{U}_R, \tilde{B}_x)) + (0, 0, 0, 0, 0, \tilde{\psi}, 0, 0, c_h^2 \tilde{B}_x)^T$$

Analogous expressions can be found for $\mathbf{G}_{i,j+\frac{1}{2}}$. Finally, we need to consider the source terms, we can use operator splitting to solve the initial value problem

$$\frac{\partial \psi}{\partial t} = -\frac{c_h^2}{c_p^2} \psi$$

or instead, we can integrate exactly for a time increment by

$$\psi^{n+1} = \psi^* \exp\left(-\Delta t \frac{c_h^2}{c_p^2}\right)$$

where ψ^* is the value of ψ obtained from the most recent step. The value of c_p has been obtained through numerical experiment, Dedner et Al [20] recommend setting

$$\frac{c_p^2}{c_h} = 0.18$$

It should be noted that the boundary conditions for ψ are set to be the same as those for ρ in every case. The initial conditions $\psi^0 = 0$.

4. Numerical Experiments

In this section, we present various validation tests to ensure the correct working of our numerical method for solving the ideal MHD equations in both 1D and 2D. The numerical method used is the dimensionally split MUSCL-Hancock with a HLLC solver as described in section 3. We also investigate the effects of divergence cleaning quantitatively. For all of the results presented a small CFL number of $C_{\text{small}} = 0.2 * C_{\text{original}}$ has been used during the first 10 - 20 iterations to avoid 'start-up errors' generated by initial discontinuities.

A. One dimensional tests

1D Sod's shock tube test To validate our 1D numerical scheme with $\mathbf{B} = 0$ we consider Sod's shock tube test [6]. This test is defined on the domain $x \in [0, 1]$. The left and right initial states are given by:

$$\begin{aligned}x \leq 0.5 & \quad \mathbf{W}_L = (1, 0, 0, 0, 1, 0, 0, 0)^T \\ x > 0.5 & \quad \mathbf{W}_R = (0.125, 0, 0, 0, 0.1, 0, 0, 0)^T\end{aligned} \quad (21)$$

We assume an ideal gas with $\gamma = 1.4$ and the test is run to a final time $t = 0.25$, with $CFL = 0.9$. Transmissive boundary conditions are used. The solution consists of a left moving rarefaction wave, a contact discontinuity and a right moving shock wave. The results for three different resolutions $N = 100, 200, 400$ using the Minbee slope limiter are shown in figures (1-4). The results reproduce the exact solutions well, as the resolution is increased the solution converges towards the exact solution.

1D Brio and Wu's shock tube test To test the implementation of the magnetic field terms, we consider Brio and Wu's shock tube test [7]. It should be noted that the initial hydrodynamic data (ρ, \mathbf{v}, p) is identical to those in Sod's test but there is a non-zero magnetic field component (i.e $\mathbf{B} \neq 0$). The test is defined on a domain $x \in [0, 800]$. The left and right initial states are defined as follows:

$$\begin{aligned} x \leq 0.5 \quad \mathbf{W}_L &= (1, 0, 0, 0, 1, 0.75, 1, 0)^T \\ x > 0.5 \quad \mathbf{W}_R &= (0.125, 0, 0, 0, 0.1, 0.75, -1, 0)^T \end{aligned} \quad (22)$$

We take $\mu_0 = 1.0$ and $\gamma = 2.0$ and the test is run to a final time $t = 80$, with $C = 0.9$. Transmissive boundary conditions are used. The solution consists of [7]; moving to the left a rarefaction wave and a slow compound wave and moving to the right a contact discontinuity, slow shock and fast rarefaction wave. The results for three different resolutions $N = 100, 200, 400$ using the Minbee slope limiter are shown in figures (5-9). The results show good agreement to those presented in [7], again as the resolution is increased the solution converges towards the exact solution. There is some diffusive behaviour but this is reduced as the resolution increases. Moreover, there is a small overshoot in the velocity. Both of these effects can be attributed to the choice of slope limiter used.

One-dimensional test: Sod Test

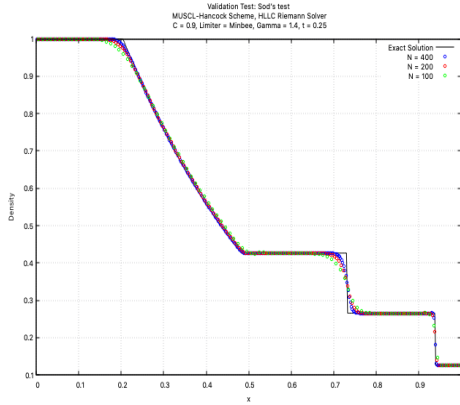


Figure 1: Density for Sod's Test, $N = 100, 200, 400$

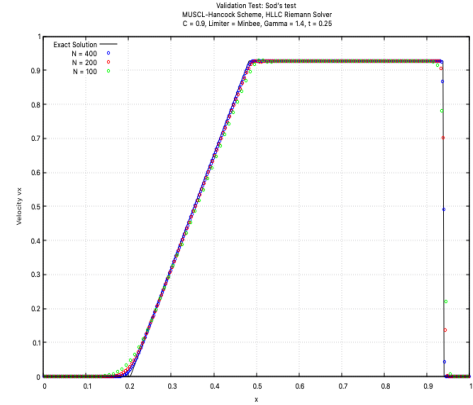


Figure 2: v_x for Sod's Test, $N = 100, 200, 400$

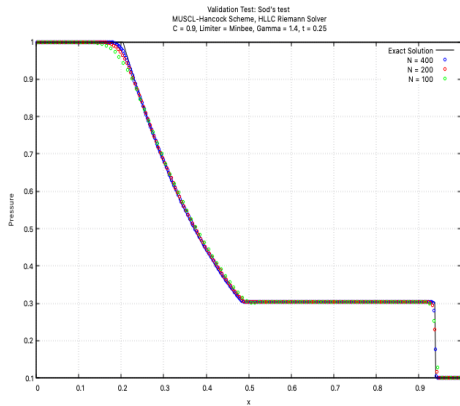


Figure 3: Pressure for Sod's Test, $N = 100, 200, 400$

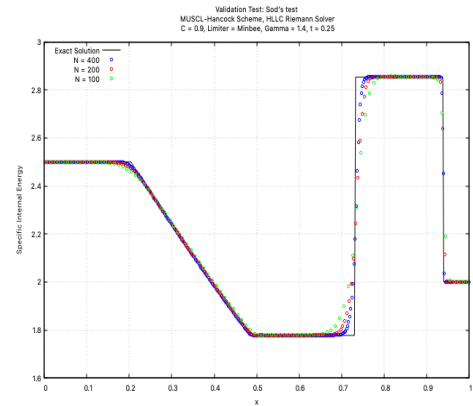


Figure 4: Internal Energy for Sod's Test, $N = 100, 200, 400$

One-dimensional test: Brio Wu Test

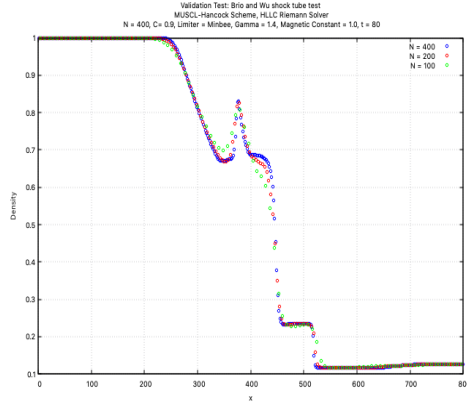


Figure 5: Density for Brio-Wu Test, $N = 100, 200, 400$

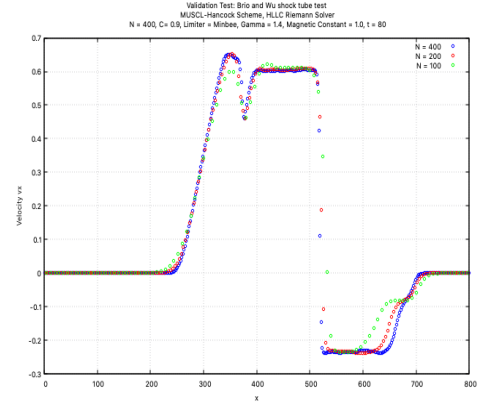


Figure 6: v_x for Brio-Wu Test, $N = 100, 200, 400$

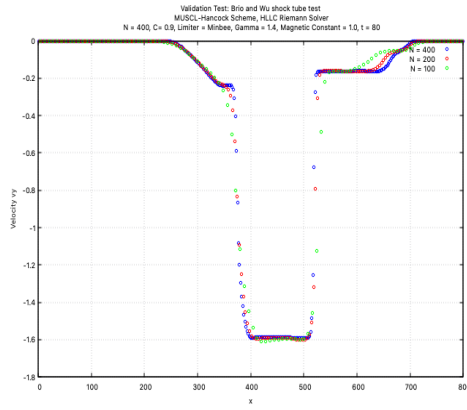


Figure 7: v_y for Brio-Wu Test, $N = 100, 200, 400$

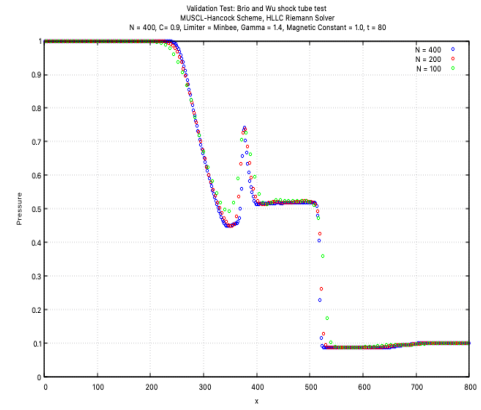


Figure 8: Pressure for Brio-Wu Test, $N = 100, 200, 400$

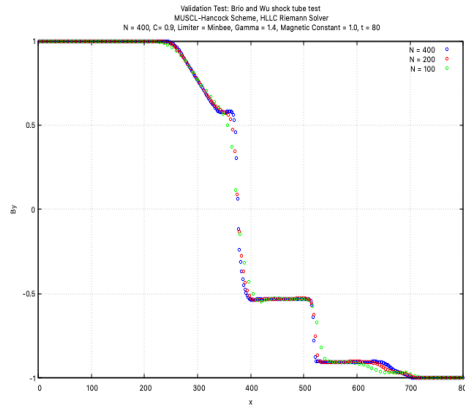


Figure 9: B_y for Brio-Wu Test, $N = 100, 200, 400$

B. Two-dimensional tests

Two dimensional and diagonally aligned Sod Test To validate our 2D numerical scheme in the case $\mathbf{B} = 0$ we consider Sod's shock tube test [6] defined on a domain $[0, 1] \times [0, 1]$ with the same initial conditions as given in (21). This is effectively a one-dimensional test. To ensure the results of the code are direction independent for the 1D test, we consider the same initial data but where the left state in (21) corresponds to $y \leq 0.5$ and the right state corresponds to $y > 0.5$. We also consider a modification of Sod's test where the initial discontinuity follows the line $y = 1 - x$. The discontinuity is chosen such that it is not perpendicular to either coordinate axis. All three versions of the tests have been run with $N = 200 \times 200$ cells with the same parameters, slope limiter and boundary conditions used as in the 1D case described earlier, in order to allow for direct comparison.

Colour map results for these three versions of Sod's tests are shown in figures 10-21. The same results as one-dimensional slices taken across the appropriate axis can be found in appendix A. The results in the x -direction are identical to those obtained in the one-dimensional case. It is clear to see that the x and y direction tests produce identical results when appropriately aligned. In the results for the diagonally aligned test as shown in figures 12,15,18,21, we see the same behaviour across most of the domain except at the boundaries/corners. This is attributed to the transmissive boundary conditions used. When using transmissive boundary conditions, the ghost cells are updated by extrapolating the values from cells within the physical domain where the flow is orthogonal and aligned. Whereas now the flow of motion is diagonal, this causes extra behaviour occurring at the corners of the domain when the waves in the simulation interact with the boundaries.

Toro Cylindrical Explosion In this test we consider Toro's Cylindrical Explosion test [6] defined on a domain $[0, 2] \times [0, 2]$. The initial data consists of a region inside a circle centred at $(1, 1)$ with a radius $R = 0.4$ and the region outside of this circle:

$$\left. \begin{aligned} \rho^{ins} &= 1.0, & \rho^{out} &= 0.125, \\ v_x^{ins} &= 0.0, & v_x^{out} &= 0.0, \\ v_y^{ins} &= 0.0, & v_y^{out} &= 0.0, \\ p^{ins} &= 1.0, & p^{out} &= 0.1. \end{aligned} \right\} \quad (23)$$

We assume an ideal gas with $\gamma = 1.4$ and the test is run to a final time $t = 0.25$, with $C = 0.9$ and $N = 101 \times 101$ cells. The slope limiter function used is Vanleer and the boundary conditions are transmissive.

The solution consists of a circular shock wave and contact discontinuity travelling away from the centre and a circular rarefaction traveling towards $(1, 1)$. Figures 22-25 show the profiles of the two-dimensional solutions. These results agree well with figure 17.4 in [6]. Furthermore, the density and pressure surface plots shown in figures 26-27 agree well with figure 17.2 and 17.3 from [6]. It is important to note that when the test is set up, the cells which are cut by the initial discontinuity should be weighted to distribute the high and low-pressure initial conditions across the cell. Our code does not implement this, hence we see small features interacting at right-angles to each other creating small amplitude waves in the solution.

Two-dimensional Brio-Wu Test To test the implementation with $\mathbf{B} \neq 0$ we consider the Brio and Wu shock tube run in both the x and y direction to ensure the code's results are direction independent. The test is defined on a domain $[0, 800] \times [0, 800]$. For the x -direction version of the test, the left and right initial states are as defined in (22). For the y -direction version, the x and y components of the magnetic field vectors are switched and the left and right initial states correspond to the discontinuity $y \leq 400$ and $y > 400$ respectively. These tests have been run with $N = 200 \times 200$ cells with the same parameters, slope limiter and boundary conditions used as in the 1D case described earlier, in order to allow for direct comparison.

The colour map results for these tests are shown in figures 28-37, the equivalent one-dimensional plots taken across the appropriate axis can be found in Appendix B. The x -direction results are identical to those obtained in the one-dimensional case. Looking at both the one-dimensional slices and colour maps, it is evident that the x and y direction tests produce identical results when appropriately aligned.

Two-dimensional Sod's Test (2D Colour Map)

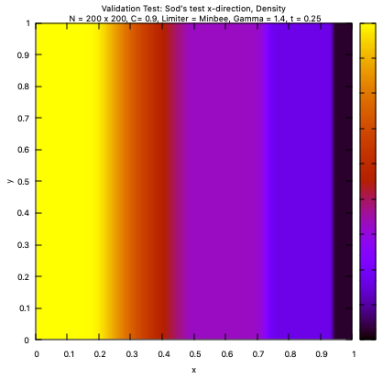


Figure 10: Density for Sod-Test x -direction

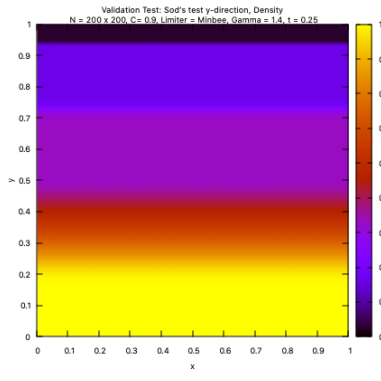


Figure 11: Density for Sod-Test y -direction

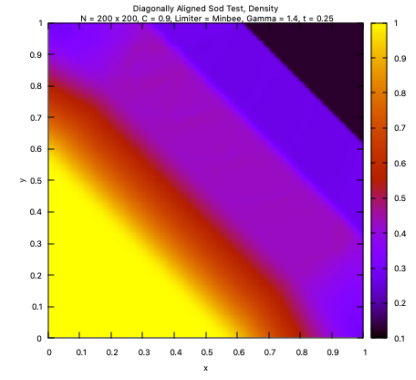


Figure 12: Density for diagonally aligned Sod-Test

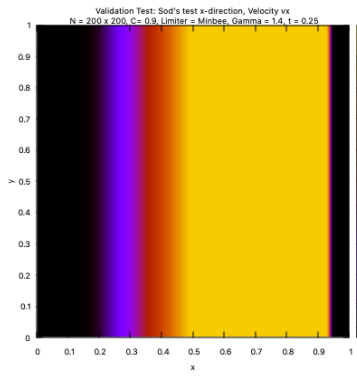


Figure 13: v_x for Sod-Test x -direction

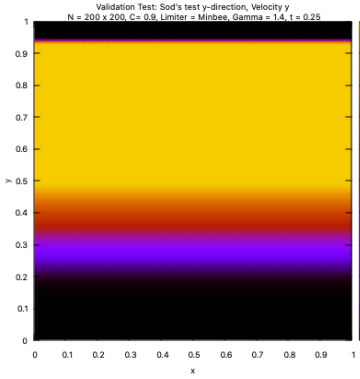


Figure 14: v_y for Sod-Test y -direction

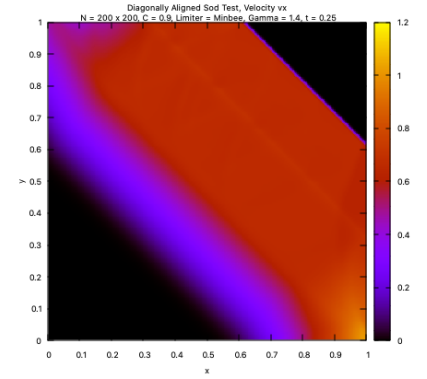


Figure 15: v_x for diagonally aligned Sod-Test

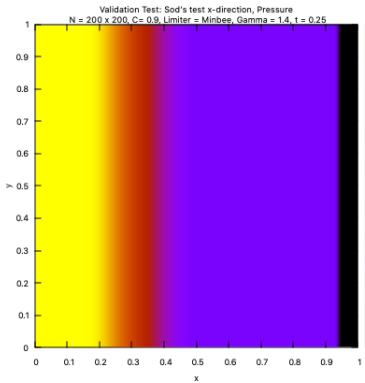


Figure 16: Pressure for Sod-Test x -direction

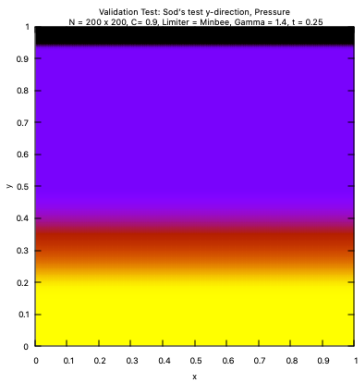


Figure 17: Pressure for Sod-Test y -direction

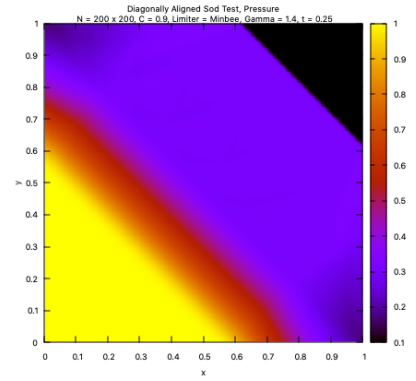


Figure 18: Pressure for diagonally aligned Sod-Test

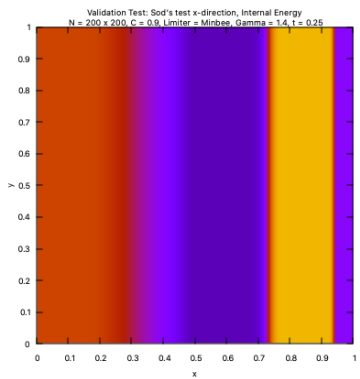


Figure 19: Internal Energy for Sod-Test x -direction

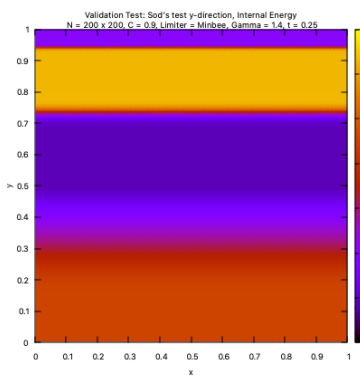


Figure 20: Internal Energy for Sod-Test y -direction

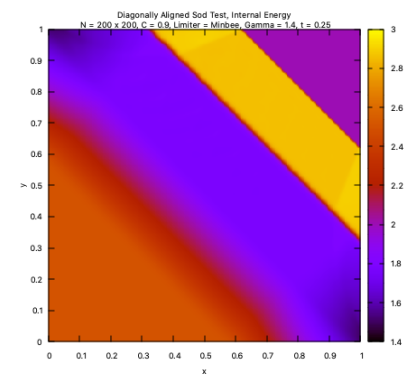


Figure 21: Internal Energy for diagonally aligned Sod-Test

Toro's Cylindrical Explosion

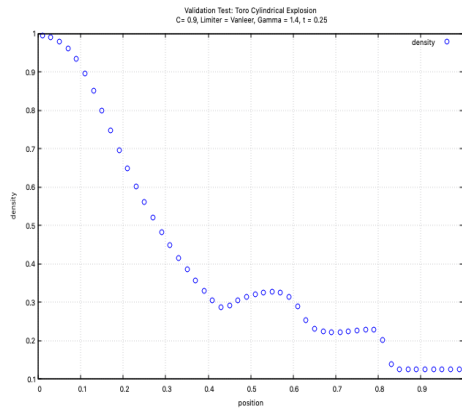


Figure 22: Density profile for Toro's Cylindrical Explosion

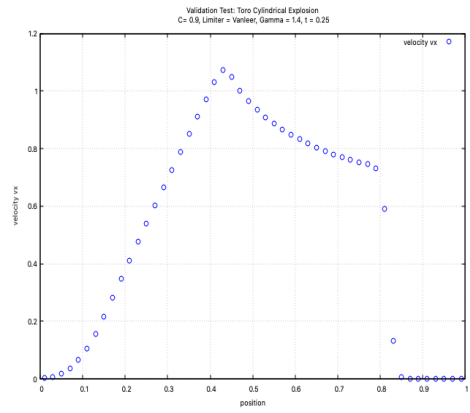


Figure 23: v_x profile for Toro's Cylindrical Explosion

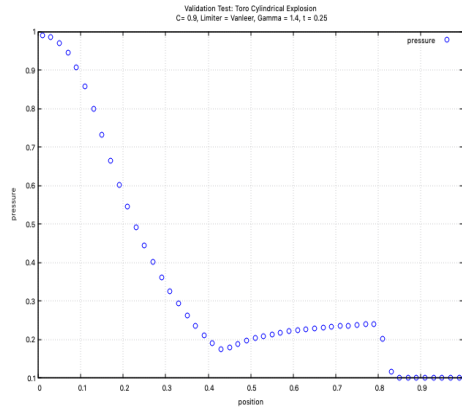


Figure 24: Pressure profile for Toro's Cylindrical Explosion

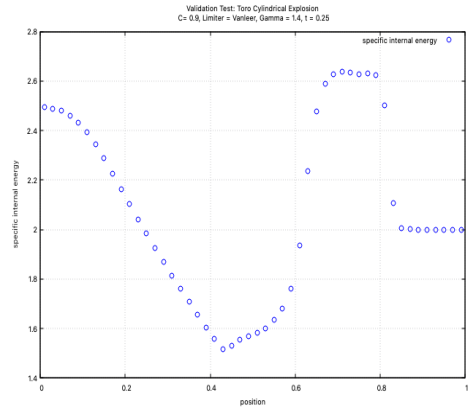


Figure 25: Internal Energy profile for Toro's Cylindrical Explosion

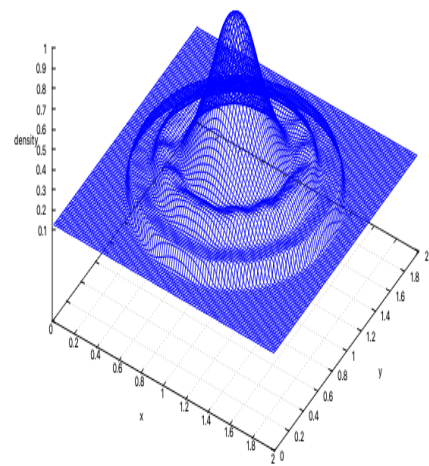


Figure 26: Density Surface Plot for Toro's Cylindrical Explosion

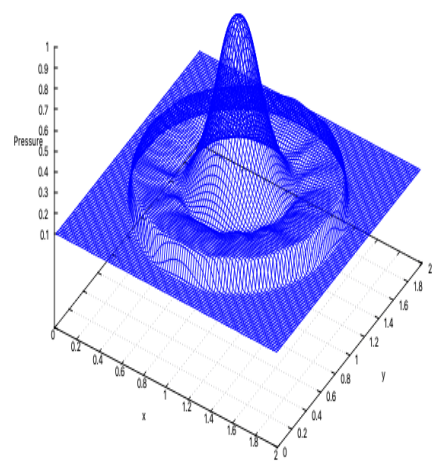


Figure 27: Pressure Surface Plot for Toro's Cylindrical Explosion

Two-dimensional Brio-Wu Test (2D Colour Map)

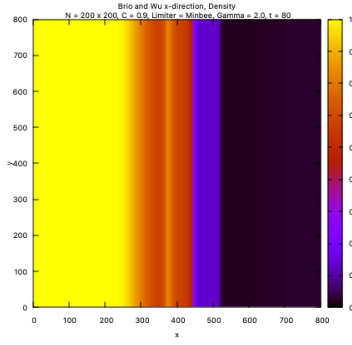


Figure 28: Density for Brio-Wu Test x -direction

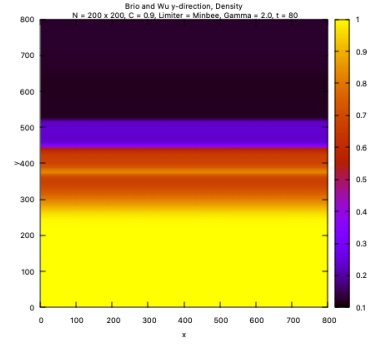


Figure 29: Density for Brio-Wu Test y -direction

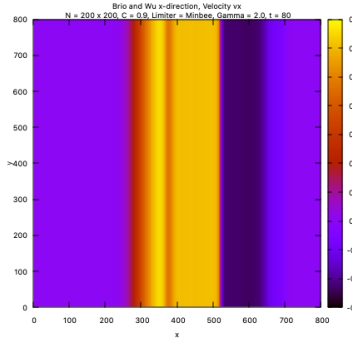


Figure 30: v_x for Brio-Wu Test x -direction

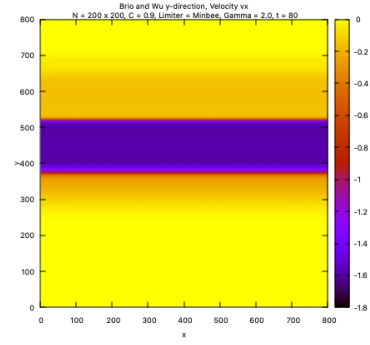


Figure 31: v_x for Brio-Wu Test y -direction

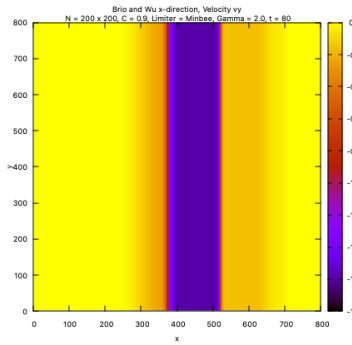


Figure 32: v_y for Brio-Wu Test x -direction

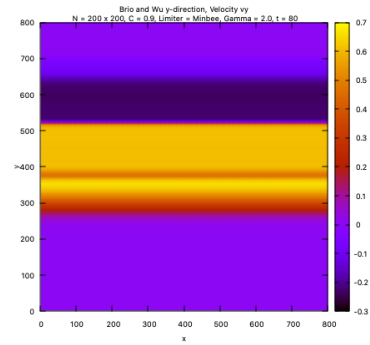


Figure 33: v_y for Brio-Wu Test y -direction

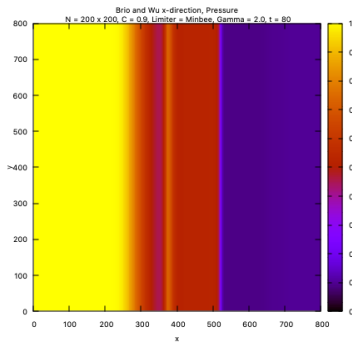


Figure 34: Pressure for Brio-Wu Test x -direction

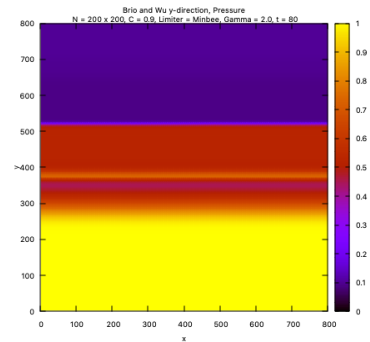


Figure 35: Pressure for Brio-Wu Test y -direction

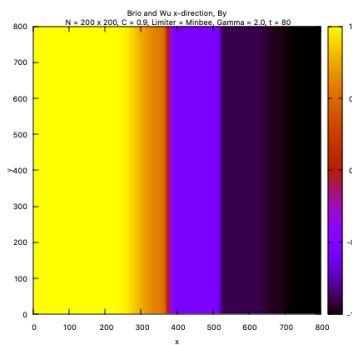


Figure 36: B_y for Brio-Wu Test x -direction

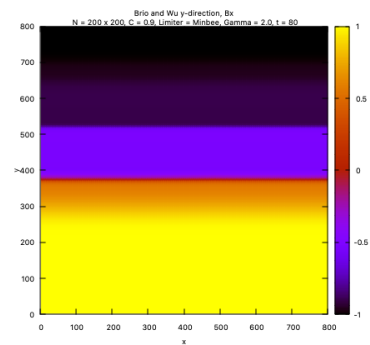


Figure 37: B_x for Brio-Wu Test y -direction

C. Novel MHD Tests and Divergence Cleaning

To test the full 2D implementation with a non-zero magnetic field we consider two novel MHD tests as described by Vides et Al [23]. In this section we also consider an extension of the 2D ideal MHD solver which incorporates Dedner et Al's [20] divergence cleaning method as described in Section 3. We present two versions of results for each novel test considered; the first obtained when no correction is applied, the second when divergence cleaning is applied to ensure the divergence-free constraint is satisfied. In this analysis, the divergence of the magnetic field \mathbf{B} for a cell (i, j, k) at time t^n is computed as [23]

$$(\nabla \cdot \mathbf{B})_{i,j,k}^n = \frac{B_{x,i+1,j,k}^n - B_{x,i-1,j,k}^n}{2\Delta x} + \frac{B_{y,i,j+1,k}^n - B_{y,i,j-1,k}^n}{2\Delta y} + \frac{B_{z,i,j,k+1}^n - B_{z,i,j,k-1}^n}{2\Delta z}$$

The L^1 norm of the divergence at time t^n is computed as

$$L^1(\nabla \cdot \mathbf{B}) = \frac{1}{N_x N_y} \sum_{i,j,k} |(\nabla \cdot \mathbf{B})_{i,j,k}^n|$$

where N_x and N_y are the number of cells in the x and y -direction respectively. It should be noted that the results for the Orszag-Tang and Kelvin Helmholtz instability will not exactly match as Vides et Al [23] use a second-order MUSCL-Hancock method with a HLLD solver to produce their results.

Orszag-Tang Test The first novel test considered is the Orszag-Tang test, this test describes a periodic fluid configuration with initial conditions which produce supersonic MHD turbulence [23]. The domain considered for this problem is $[0, 1] \times [0, 1]$, $\gamma = \frac{5}{3}$ and the boundary conditions are taken to be periodic. The initial conditions are given by

$$\mathbf{W}(x, y) = \begin{bmatrix} \gamma^2 \\ -\sin(2\pi y) \\ \sin(2\pi x) \\ 0 \\ \gamma \\ -\sin(2\pi y) \\ \sin(4\pi x) \\ 0 \end{bmatrix}$$

For this test $N = 256 \times 256$ cells are used, with $C = 0.9$ and the choice of limiter is Minbee. The plots for density at $t = 0.5$ and $t = 1.0$ are shown in figures 38 and 39, these seem to agree well with the results of Vides et Al in the case of no correction to the divergence-free

condition. Figures 40-41 show the results when mixed correction divergence cleaning is used. When divergence cleaning is used there is little change at $t = 0.5$ as the errors have not significantly accumulated yet. However at $t = 1.0$ divergence cleaning has some effect on the behaviour of density in the middle and close to the left and right boundaries of the plot. Figure 42 shows the evolution of the L^1 norm of the divergence $\nabla \cdot \mathbf{B}$ for the no-correction and divergence cleaning approaches. It is evident to see that the measured L^1 norm errors increase as time progresses when no-correction is applied, the errors are significantly reduced and tend to 0 when divergence cleaning is used.

Kelvin-Helmholtz Instability The second novel test considered is the Kelvin Helmholtz instability, this test is useful in demonstrating the importance of divergence cleaning. The domain considered for this problem is $[0, 1] \times [-1, 1]$ and $\gamma = \frac{5}{3}$. The boundary conditions are taken to be reflexive on the top and bottom of the domain and periodic on the left and right of the domain. The initial conditions are given by

$$\mathbf{W}(x, y) = \begin{bmatrix} 1 \\ 0.5 \tanh(20y) \\ 0.01 \sin(2\pi x) \exp\left(-\frac{y^2}{0.1^2}\right) \\ 0 \\ 0.1 \cos(\pi/3) \\ 0.0 \\ 0.1 \sin(\pi/3) \\ 1/\gamma \end{bmatrix}$$

For this test $N = 256 \times 256$ cells are used, with $C = 0.9$ and the choice of limiter is Minbee. The plots for this test are produced at $t = 5, 8, 12, 20$ seconds for the ratio of the poloidal field strength and the toroidal component $\sqrt{B_x^2 + B_y^2}/B_z$. The results produced when no correction is applied to the divergence field are given in figures 43-46. We see good agreement of the results at early times and see the formation of the cat eye vortex, at later times we see the effects of the divergence errors in play. This is expected in the case of no correction. The results produced when mixed GLM divergence cleaning is applied to the divergence field are given in figures 47-50. We see good agreement with the results presented in Vides et Al. Figure 51 shows the evolution of the L^1 norm of the divergence $\nabla \cdot \mathbf{B}$ for the no-correction and divergence cleaning approaches. It is evident to see that the measured L^1 norm errors for this test rapidly increase when no-correction is applied. Again the measured errors are significantly reduced and tend to 0 when divergence cleaning is used.

Orszag Tang Test

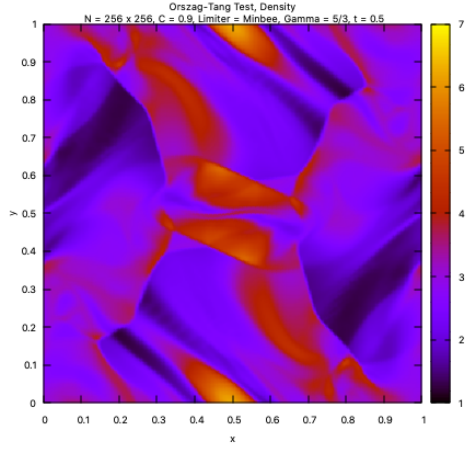


Figure 38: Density, $t = 0.5$

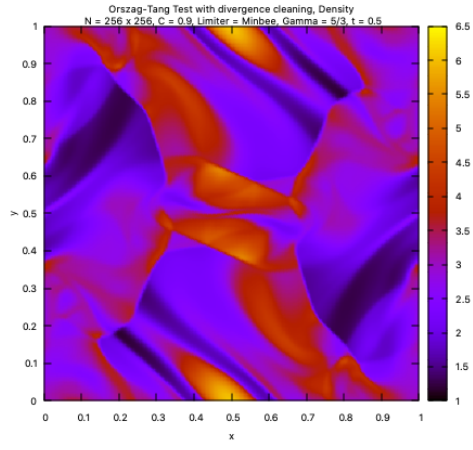


Figure 39: Density with divergence cleaning, $t = 0.5$

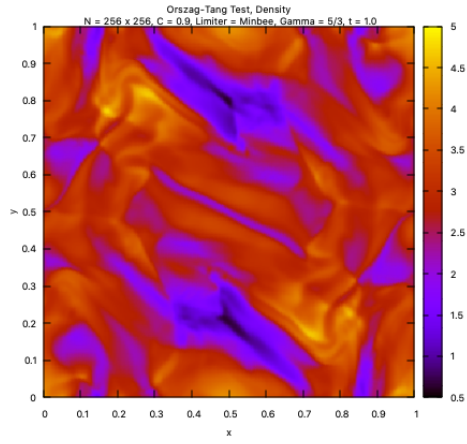


Figure 40: Density, $t = 1.0$

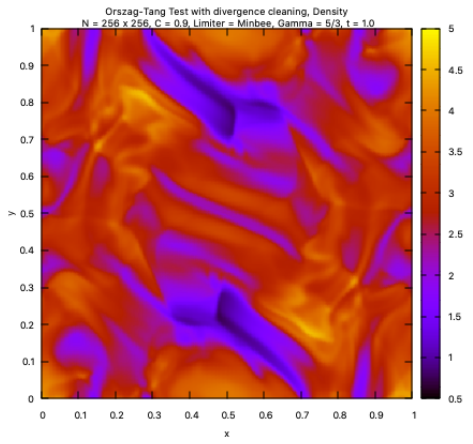


Figure 41: Density with divergence cleaning, $t = 1.0$

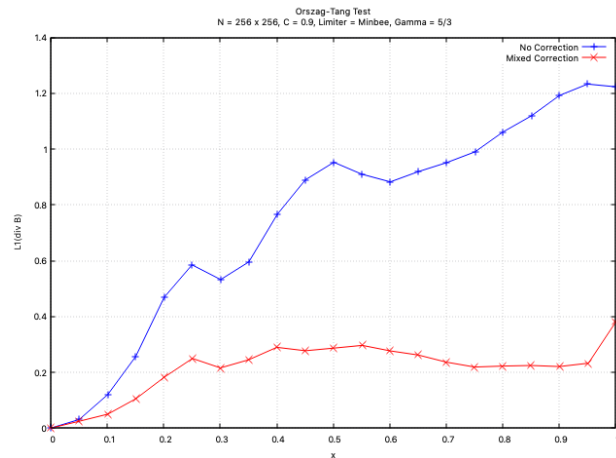


Figure 42: Comparison of $L^1(\nabla \cdot \mathbf{B})$ for Orszag-Tang test with no correction and with divergence cleaning

Kelvin Helmholtz Instability

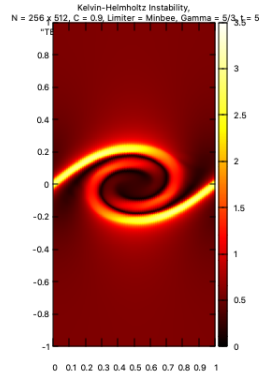


Figure 43: No correction, $t = 5$

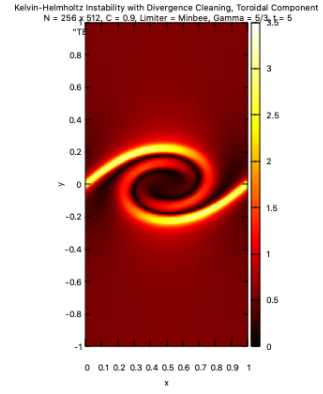


Figure 47: Divergence Cleaning, $t = 5$

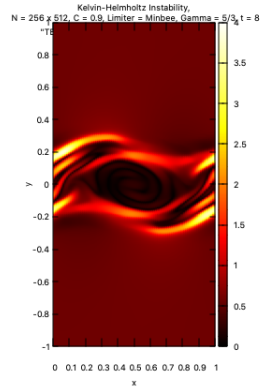


Figure 44: No correction, $t = 8$

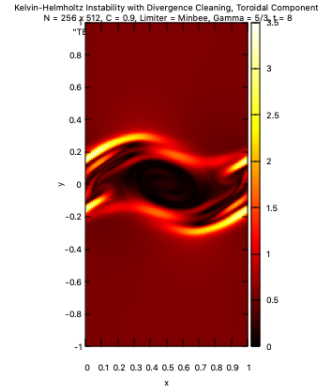


Figure 48: Divergence Cleaning, $t = 8$

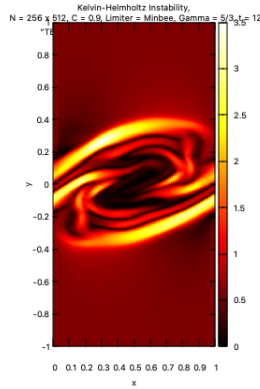


Figure 45: No correction, $t = 12$

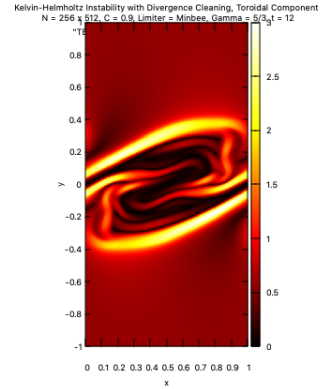


Figure 46: Divergence Cleaning, $t = 12$

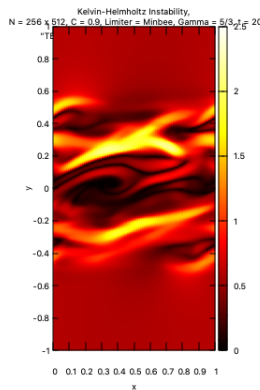


Figure 49: No correction, $t = 20$

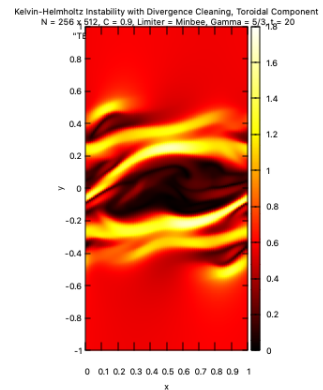


Figure 50: Divergence Cleaning, $t = 20$

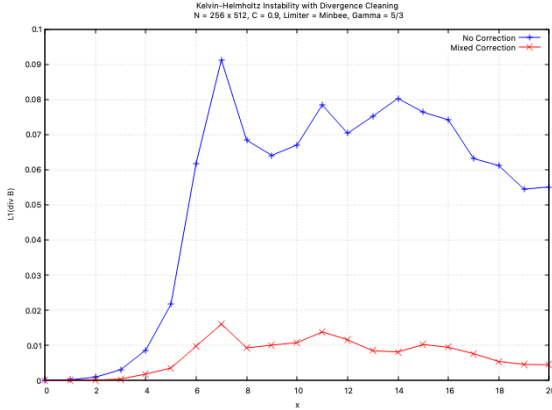


Figure 51: Comparison of $L^1(\nabla \cdot \mathbf{B})$ for Kelvin-Helmholtz Instability with no correction and with divergence cleaning

5. Conclusion

In this work, a high-resolution Riemann-problem based method has been used to numerically solve the compressible ideal magnetohydrodynamics equations in 1D and 2D. This was accomplished by combining a MUSCL-Hancock scheme with the HLLC Riemann Solver of Li [17]. We have considered a series of validation tests and have been able to reproduce the results of several authors [7][6][23]. Furthermore, the scheme has been extended to incorporate the divergence cleaning method, devised by Dedner et Al [20] which aims to maintain the divergence-free property of the magnetic field. In particular we have considered the mixed GLM approach proposed by Dedner et Al which propagates divergence errors to the boundaries of the domain whilst simultaneously damping the errors. We have compared the effects between using the divergence cleaning vs using no correction on simulating novel MHD problems both qualitatively and quantitatively. It is clear to see that the mixed GLM approach significantly reduces numerical errors which if left unchecked can grow overtime and lead to instability and generate unphysical behaviour in the solution.

Following this work, our numerical scheme can be extended in a number of ways. For example, we can consider other divergence cleaning ansatz such as the hyperbolic and parabolic correction approaches [20]. An advantage of the divergence cleaning method is that it is easy to incorporate in any existing code and it preserves the conservation of the internal energy [23]. However, the effectiveness of this numerical technique depends on tunable parameters. Suitable values for the parabolic correction constant c_p have been recommended by Ded-

ner et Al and have been obtained through numerical experiments. In future work, we aim to consider the performance of other techniques such as the constrained transport technique where the divergence constraint is built into the numerical method and is therefore mathematically more accurate.

The divergence cleaning approach requires a Riemann problem based numerical technique. In this paper, we have considered a HLLC solver proposed by Li to solve the ideal MHD equations. As the ideal MHD system is non-convex and not strictly hyperbolic [7], apart from shocks and rarefactions, wave structures such as rotational discontinuities and compound waves can exist. A limitation of the HLLC solver is that it cannot resolve isolated discontinuities. In future work, we aim to extend our study to solve the ideal MHD equations using an approximate Riemann solver such as HLLD which better captures waves present in the ideal MHD system and get a more accurate solution.

Additionally, we aim to extend our work beyond ideal MHD such as incorporating models with resistivity and incorporating relativistic effects in order to cover more physical problems. We could also improve the order of accuracy of our current scheme by considering using higher-order solvers such as ENO etc.

Appendix A. Two-dimensional Sod Test (one-dimensional slices)

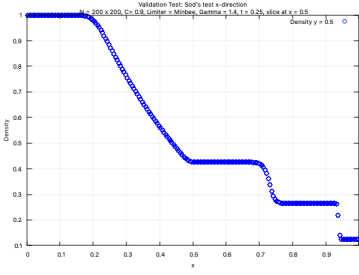


Figure A.52: Density for Sod-Test x -direction, slice $y = 0.5$

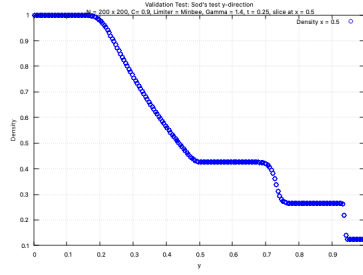


Figure A.53: Density for Sod-Test y -direction, slice $x = 0.5$

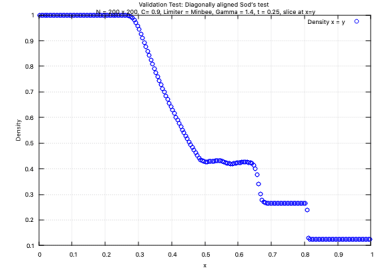


Figure A.54: Density for diagonally aligned Sod-Test, slice $x = y$

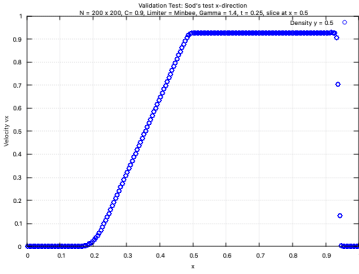


Figure A.55: v_x for Sod-Test x -direction, slice $y = 0.5$

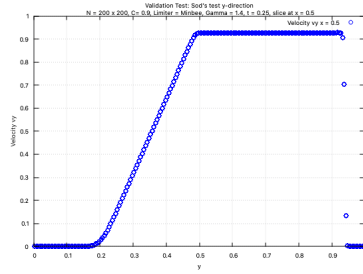


Figure A.56: v_y for Sod-Test y -direction, slice $x = 0.5$

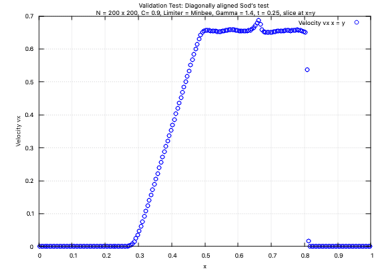


Figure A.57: v_x for diagonally aligned Sod-Test, slice $x = y$

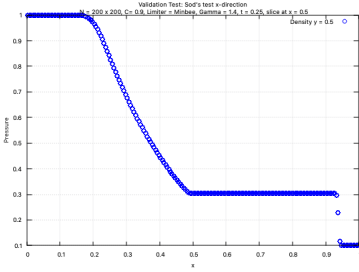


Figure A.58: Pressure for Sod-Test x -direction, slice $y = 0.5$

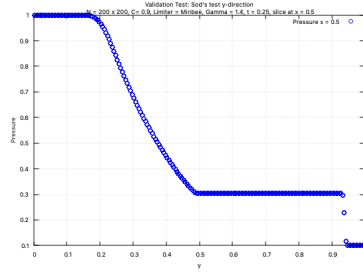


Figure A.59: Pressure for Sod-Test y -direction, slice $x = 0.5$

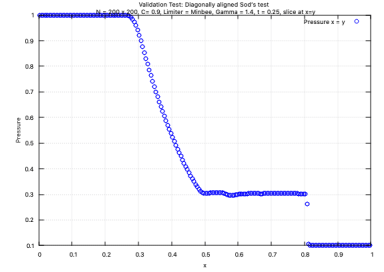


Figure A.60: Pressure for diagonally aligned Sod-Test, slice $x = y$

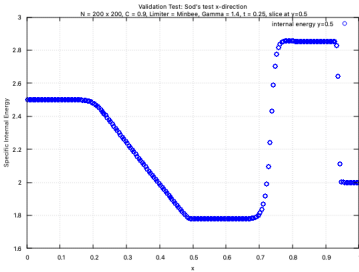


Figure A.61: Internal Energy for Sod-Test x -direction, slice $y = 0.5$

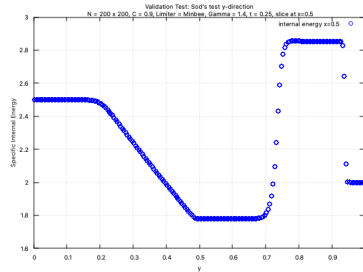


Figure A.62: Internal Energy for Sod-Test y -direction, slice $x = 0.5$

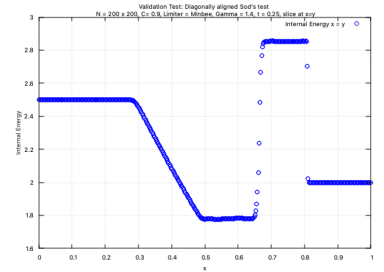


Figure A.63: Internal Energy for diagonally aligned Sod-Test, slice $x = y$

Appendix B. Two-dimensional Brio-Wu Test (one-dimensional slices)

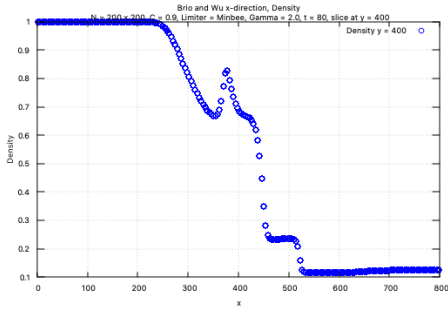


Figure B.64: Density for x -direction test, slice $y = 400$

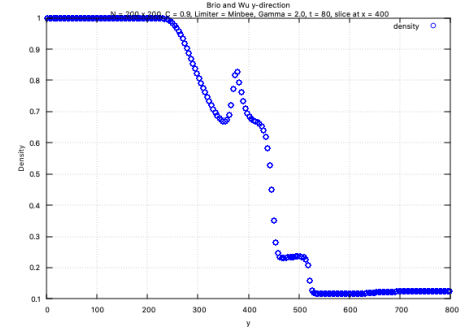


Figure B.65: Density for y -direction test, slice $x = 400$

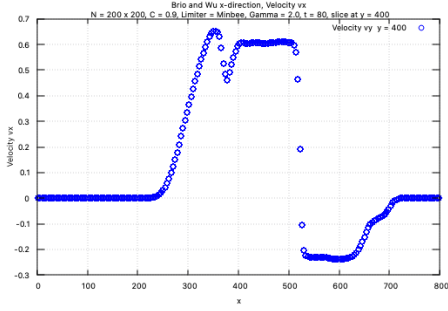


Figure B.66: v_x for x -direction test, slice at $y = 400$

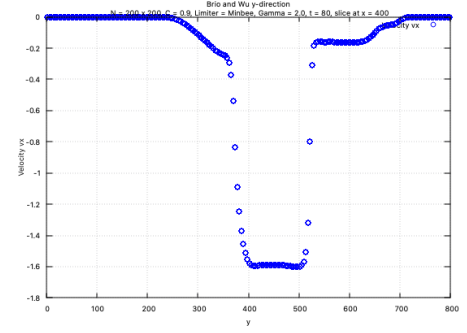


Figure B.67: v_x for y -direction test, slice at $x = 400$

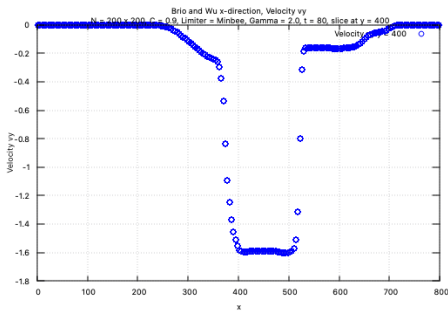


Figure B.68: v_y for x -direction test, slice at $y = 400$

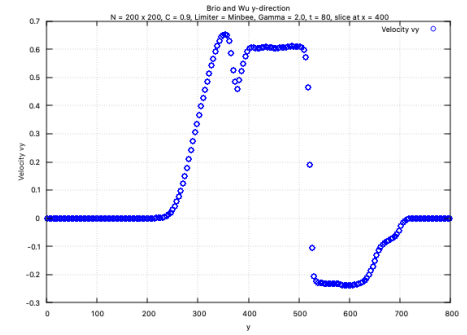


Figure B.69: v_y for y -direction test, slice at $x = 400$

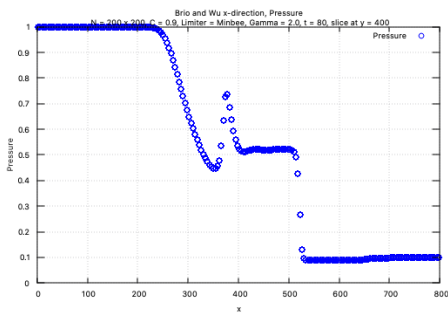


Figure B.70: Pressure for x -direction test, slice at $y = 400$

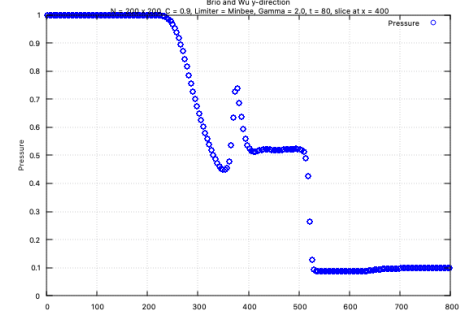


Figure B.71: Pressure for y -direction test, slice at $x = 400$

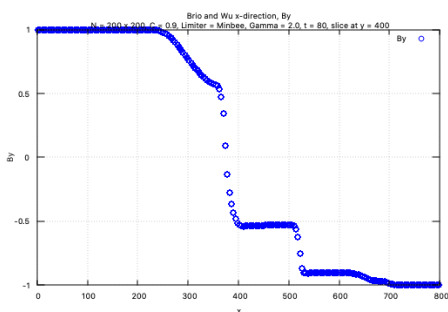


Figure B.72: B_y for x -direction test, slice at $y = 400$

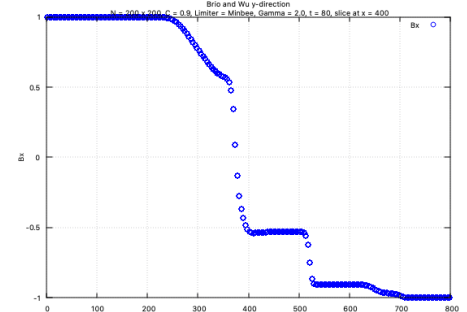


Figure B.73: B_x for y -direction test, slice at $x = 400$

References

- [1] S. Possanner, E. Sonnendrücker, Computational Plasma Physics, Lecture Notes, Max-Planck-Institut für Plasmaphysik und Zentrum Mathematik, TU München (May 2020).
- [2] ITER, ITER: In a few lines (2020).
URL <https://www.iter.org/proj/inafewlines>
- [3] B. Koren, U. Ebert, T. Gombosi, H. Guillard, R. Keppens, D. Knoll, Computational plasma physics (introduction to special issue), Journal of Computational Physics 231 (3) (2012) 717–. doi:10.1016/j.jcp.2011.11.012.
- [4] L. M. Stephen Millmore, N. Nikiforakis, Advanced Continuum Modelling Lecture Notes, Laboratory for Scientific Computing, University of Cambridge (October 2020).
- [5] Computational Methods in Plasma Physics 2020 Graduate Summer School, Princeton Plasma Physics Laboratory.
URL <https://cmpp.readthedocs.io/en/latest/>
- [6] E. F. Toro, Riemann solvers and numerical methods for fluid dynamics: A practical introduction, 2nd Edition, Springer, 1999.
- [7] M. Brio, C. Wu, An upwind differencing scheme for the equations of ideal magnetohydrodynamics, Journal of Computational Physics 75 (2) (1988) 400–422. doi:10.1016/0021-9991(88)90120-9.
- [8] D. Balsara, Linearized formulation of the riemann problem for adiabatic and isothermal magnetohydrodynamics, The Astrophysical Journal Supplement Series 116 (2009) 119. doi:10.1086/313092.
- [9] P. Cargo, G. Gallice, Roe matrices for ideal mhd and systematic construction of roe matrices for systems of conservation laws, Journal of Computational Physics 136 (2) (1997) 446–466. doi:https://doi.org/10.1006/jcph.1997.5773.
- [10] B. Einfeldt, C. Munz, P. Roe, B. Sjögreen, On godunov-type methods near low densities, Journal of Computational Physics 92 (2) (1991) 273–295. doi:https://doi.org/10.1016/0021-9991(91)90211-3.
- [11] T. Miyoshi, K. Kusano, A multi-state hll approximate riemann solver for ideal magnetohydrodynamics, Journal of Computational Physics 208 (1) (2005) 315–344. doi:https://doi.org/10.1016/j.jcp.2005.02.017.
- [12] K. Wu, C.-W. Shu, Provably positive high-order schemes for ideal magnetohydrodynamics: Analysis on general meshes, Numerische Mathematik 142 (2019) 995–1047. doi:10.1007/s00211-019-01042-w.
- [13] P. Janhunen, A positive conservative method for magnetohydrodynamics based on hll and roe methods, Journal of Computational Physics 160 (2000) 649–661. doi:10.1006/jcph.2000.6479.
- [14] T. Linde, A practical, general-purpose, two-state hll riemann solver for hyperbolic conservation laws, International Journal for Numerical Methods in Fluids 40 (2002) 391 – 402. doi:10.1002/fld.312.
- [15] K. Gurski, An hllc-type approximate riemann solver for ideal magnetohydrodynamics, SIAM J. Sci. Comput. 25 (2004) 2165–2187.
- [16] M. S. . W. S. E. F. Toro, Restoration of the contact surface in the hll-riemann solver, Shock Waves 4 (1994) 25–34.
- [17] S. Li, An hllc riemann solver for magneto-hydrodynamics, Journal of Computational Physics 203 (1) (2005) 344–357. doi:https://doi.org/10.1016/j.jcp.2004.08.020.
- [18] M. Wesenberg, Efficient mhd riemann solvers for simulations on unstructured triangular grids, Journal of Numerical Mathematics 10 (01 2002). doi:10.1515/JNMA.2002.37.
- [19] J. Brackbill, D. Barnes, The effect of nonzero γ on the numerical solution of the magnetohydrodynamic equations, Journal of Computational Physics 35 (3) (1980) 426–430. doi:https://doi.org/10.1016/0021-9991(80)90079-0.
- [20] A. Dedner, F. Kemm, D. Kröner, C.-D. Munz, T. Schnitzer, M. Wesenberg, Hyperbolic divergence cleaning for the mhd equations, Journal of Computational Physics 175 (2) (2002) 645–673. doi:https://doi.org/10.1006/jcph.2001.6961.
- [21] C. R. Evans, J. F. Hawley, Simulation of magnetohydrodynamic flows: A constrained transport model, Astrophysical Journal 332 (1998) 659.
- [22] K. G. Powell, An approximate riemann solver for magnetohydrodynamics (that works in more than one dimension), NASA Langley Research Center.
URL <https://ntrs.nasa.gov/citations/19940028527>
- [23] J. Vides, E. Audit, H. Guillard, B. Nkonga, Divergence-free mhd simulations with the heracles code, Esaim: Proceedings 43 (2013) 180–194.